Examination of vorticity and divergence on a rotating turbulent convection model of Jupiter's polar vortices

Tao Cai

[1]State Key Laboratory of Lunar and Planetary Sciences, Macau University of Science and Technology, Macau, P.R.China

Key Points:

- Deep convection model shows that the divergence and vorticity are correlated in the polar vortices of Jupiter.
- The correlation varies with the depth of the atmosphere and the resolution of the measurement.
- The polar vortices at the top of atmosphere are likely sustained by the transfer of vorticity from deeper layers.

Corresponding author: Tao Cai, tcai@must.edu.mo, astroct@gmail.com

Abstract

The correlation between divergence and vorticity has traditionally served as a signature of convection in rotating fluids. While this correlation has been observed in the JIRAM brightness temperature data for Jupiter's polar vortices, it is notably absent in the JIRAM images. This discrepancy presents a new challenge in determining whether this correlation can serve as a reliable signature of convection in rapidly rotating atmospheres. In this study, we analyzed data from a three-dimensional simulation of Jupiter's polar vortices using a deep convection model. Our findings confirm the theoretical prediction of a negative correlation between divergence and vorticity in the northern hemisphere. Interestingly, this correlation is weaker within the cyclones compared to outside them. The skewness of upflows and downflows plays an important role in this negative correlation. We also observed that the correlation varies with height, being strongest near the interface and decaying away from it. The correlation diminishes when the resolution is reduced. Furthermore, our findings suggest that the geostrophic approximation may not be suitable for the Jovian atmosphere, particularly in the stable layer. Both tilting and stretching effects contribute to the material derivative of vorticity, with the tilting effect dominating in the unstable layer and the stretching effect prevailing in the stable layer. This suggests a transfer of vorticity from the convectively unstable layer to the stable layer. Consistent with observations, we also noted an upscale energy transfer from smaller to larger scales.

Plain Language Summary

Jupiter has fascinating polar vortices on its poles. But how do they form, how deep are they, and how do they survive? Answering these questions will not only enhance our understanding of Jupiter's weather patterns but also provide insights into the climatic conditions on our own planet, Earth. In this study, we employ a deep convection model to elucidate the formation of these vortices. By analyzing the simulation data, we can ascertain whether the observed data at the top of the atmosphere bear signatures from deep within. Divergence, which quantifies the tendency of fluid to accumulate or disperse at a point, and vorticity, which measures the tendency of fluid to swirl around a point, are key parameters in our analysis. The correlation between these two parameters can serve as a signature of convection. Indeed, our simulation identifies this signature. However, its strength varies with the depth of the atmosphere and the resolution of the measurement. Furthermore, our findings suggest that the spin of the polar vortices at the top of the atmosphere is likely maintained by the transfer of vorticity from the deeper layers of the atmosphere.

1 Introduction

The Juno mission has unveiled intriguing polygonal patterns of closely packed large-scale cyclones on Jupiter's poles (Adriani et al., 2018; Tabataba-Vakili et al., 2020). This discovery of closely packed polar vortices poses a challenging problem in comprehending the dynamics of the Jovian atmosphere. Two scenarios have been put forth to elucidate the formation of polar cyclones in gas giants: the shallow model and the deep model. The shallow model posits that these polar cyclones are a product by moist convection in the shallow weather layer of gas giants(Zhang & Showman, 2014; O'Neill et al., 2015), while the deep model advocates that they are formed by rotating convection in the deep atmosphere of the planets (Yadav & Bloxham, 2020; Cai et al., 2021). Despite the difference between the deep and shallow models, convection is increasingly being recognized as the probable origin of these large-scale polar cyclones.

Early simulations in three-dimensional compressible flow have indicated the potential mechanism on the formation of large-scale vortices in rapidly rotating convection (K. Chan, 2007). This observation was later substantiated by subsequent simulations conducted

on rotating compressible convection within f-boxes (Käpylä et al., 2011; K. L. Chan & Mayr, 2013; Cai, 2016). Moreover, K. L. Chan and Mayr (2013) identified a state transition from large-scale cyclones to large-scale anticyclones with increasing rotation rates. Subsequent simulations on incompressible flow also validated the mechanism for generating large-scale vortices in rapidly rotating convection (Julien et al., 2012; Guervilly et al., 2014; Favier et al., 2014; Rubio et al., 2014; Kunnen et al., 2016; Cai, 2021). It has been confirmed that the formation of large-scale vortices in rotating convection requires two conditions to be met: sufficient turbulence and rapid rotation (Guervilly et al., 2014; Favier et al., 2014; Cai, 2021). Recently, this mechanism has been utilized to explain the formation of Jupiter's polar cyclones and the Great Red Spot (Cai et al., 2021, 2022). Based on the data from observations and simulations, Cai et al. (2022) postulated that if rapidly rotating convection is the driving force, both Jupiter's polar vortices and the Great Red Spot should extend deeper than $500km$. For the first time, Cai et al. (2021) demonstrated that the polygonal pattern of closely packed large-scale cyclones observed at Jupiter's poles can be naturally reproduced through rapidly rotating convection in a polar gamma box. The process begins with the generation of small-scale vortices, which subsequently merge and expand to form large-scale cyclones. The polar beta effect then pushes these polar cyclones into the pole to form a polygonal pattern.

In addition to three-dimensional deep convection models, a number of two-dimensional models have been employed to investigate polar cyclones in gas giants (O'Neill et al., 2015; Brueshaber et al., 2019; Li et al., 2020; Siegelman, Young, & Ingersoll, 2022). These models incorporate a simple parameterization scheme to simulate the moist convection present in the weather layer. Some of these shallow models also apply the concept of rapidly rotating convection, as demonstrated in Rayleigh Bénard convection (Guervilly et al., 2014), to account for the formation of large-scale vortices in Jupiter through moist convection. However, the driving mechanism of large-scale vortices in Rayleigh Bénard convection necessitates that the convective Rossby number, defined as the ratio of convective velocity to the product of the depth of convective flow and the Coriolis parameter, be less than a critical value (Guervilly et al., 2014; Cai, 2021). It remains uncertain whether the convective Rossby number can be sufficiently small to reach this critical value in a shallow weather layer. For instance, the simulation by Cai et al. (2022) suggests that a depth of $500km$ in the Jovian atmosphere is needed to achieve this critical value. The verification of this mechanism by moist convection calls for a more sophisticated three-dimensional shallow water model.

While numerical simulations provide compelling evidence that these polar cyclones are likely deeply rooted, verifying this hypothesis through observation remains a formidable challenge. Given the difficulty of directly measuring the vertical structure, analyses primarily focus on the horizontal structure of these cyclones. Efforts have been made to understand the dynamic processes by examining horizontal velocities. A recent analysis revealed an energy inverse cascade within the polar cyclones, mirroring observations in simulations of rotating turbulent convection (Siegelman, Klein, et al., 2022). Another approach has involved analyzing the divergence and vorticity in polar cyclones (Ingersoll et al., 2022). In turbulent convection, when the convective updraft generated in the unstable layer encounters the stable layer, it diverges and becomes anticyclonic due to the Coriolis effect, correlating the horizontal divergence and vertical vorticity (Hathaway, 1982). The relationship between divergence and vorticity has been studied extensively in the field of solar convection (Wang et al., 1995; Rüdiger et al., 1999; Gizon & Duvall Jr, 2003; Egorov et al., 2004; Komm et al., 2007, 2021). Studies have revealed a notable correlation in solar convection, exhibiting a negative trend in the northern hemisphere and a positive one in the southern hemisphere.

The flow pattern in solar convection consists of granular cells characterized by strong, concentrated downflow lanes and weak, expansive upflows (Brummell et al., 1996). In conditions of weak rotation, the cellular structure remains largely unaltered, thereby p-

reserving the validity of the aforementioned relationship between divergence and vorticity. However, Jupiter rotates at a significantly higher speed than the Sun. This rapid rotation influences the flow pattern of the Jovian atmosphere, which is dominated by jets and vortices. Given the stark contrast in flow patterns, it is uncertain whether the relationship observed in solar convection holds true in the Jovian atmosphere. Ingersoll et al. (2022) conducted a detailed examination of the correlation between vorticity and divergence within and in the vicinity of the cyclones at Jupiter's north pole, considering scales as small as 200km. They did not observe the negative correlation as expected in rotating convection.

In this paper, we investigate the relationship between divergence and vorticity on Jupiter's polar cyclones, utilizing our three-dimensional simulations as a basis. Our investigation seeks to address several key questions. Firstly, we examine whether the correlation persists in rapidly rotating convection, particularly in the presence of large-scale cyclones. Secondly, we explore the impact of varying resolutions and depth of atmosphere on these correlations. Thirdly, we investigate how the energy and vorticity transfer to sustain the large-scale cyclones.

2 The model

Using a compressible turbulent model, Cai et al. (2021) were able to successfully generate polar vortices that closely resemble those on Jupiter's poles. In this study, we extend their work by continuing to run the model and collecting the simulation data for further analysis. After ignoring the viscous term and the horizontal Coriolis parameter, the vertical component of vorticity equation for compressible flow in the polar region can be described as

$$D_t(\xi + f) = \underbrace{(\boldsymbol{\xi}_h \cdot \boldsymbol{\nabla}_h)w}_{\text{tilting term}} - \underbrace{(\xi + f)\delta}_{\text{stretching term}} + \underbrace{\rho^{-2}\boldsymbol{\nabla}_h\rho \times \boldsymbol{\nabla}_h p}_{\text{baroclinic term}} , \tag{1}$$

where $D_t = \partial_t + \boldsymbol{u} \cdot \boldsymbol{\nabla}$ is the material derivative, $\boldsymbol{u}$ is the velocity, ξ is the vertical component of vorticity, $\boldsymbol{\xi_h}$ is the horizontal component of vorticity, $\delta = \boldsymbol{\nabla}_h \cdot \boldsymbol{u}_h$ is the horizontal divergence, f is the Coriolis parameter, ρ is the density, and p is the pressure. The vorticity equation indicates that the material derivative of the vertical component of absolute vorticity can be contributed by three effects: the tilting effect, the stretching effect, and the baroclinic effect. Measuring the vertical velocity, density, and pressure from observation is challenging, making it difficult to evaluate the tilting effect and baroclinic effect. However, the horizontal velocity can be measured from observation, allowing the stretching term to be estimated. Since f is almost constant and the mean of δ is almost zero, the stretching effect can be approximated by the divergence-vorticity correlation, which is defined as the cross-correlation between ξ and δ

$$\widetilde{C}(\delta, \xi) = \langle \delta \times \xi \rangle = \frac{\iint_S \delta \times \xi dS}{\iint_S dS} , \tag{2}$$

where the symbol $\langle \cdot \rangle$ denotes the horizonal average over the region of the horizonal plane S at a specific height. The correlation coefficient between δ and ξ, which is normalized by their standard deviations, can be defined as

$$C(\delta, \xi) = \frac{\langle \delta \times \xi \rangle}{\langle \delta^2 \rangle^{1/2} \langle \xi^2 \rangle^{1/2}} . \tag{3}$$

Hence the sign of the correlation $\widetilde{C}(\delta, \xi)$ or $C(\delta, \xi)$ provides insights on whether the stretching effect contributes to the change of absolute vorticity. Similarly, we can define the correlation coefficient between the vertical velocity and the horizontal vorticity, denoted as $C(w, \delta)$, as well as the correlation coefficient between the vertical velocity and the vorticity, represented as $C(w, \xi)$.

Under the anelastic approximation, the horizontal divergence is linked to the vertical momentum through the relation $\delta = wH_m$, where $H_m = -\partial_z \ln|\rho w|$ represents the scale height for the vertical momentum, as described in Rüdiger et al. (1999). At the top of the convection zone, the value of H_m is usually positive. This is because the vertical momentum of an updraft (downdraft) tends to decrease with increasing height when it injects into (ejects from) the boundary. On the other hand, H_m is usually negative at the bottom of the convection zone. This is attributed to the fact that the vertical momentum of updraft (downdraft) tends to decrease with decreasing height.

Cai et al. (2021) conducted simulations of polar cyclones using a two-layer structure. This structure consisted of a convectively stable layer positioned above a lower unstable layer. When the upward (downward) convective flow is injected into (ejected from) the interface between these two layers, it diverged (converged), resulting in a positive (negative) horizonal divergence δ (see the left panel of Fig. 1 for the illustration). Flow that is divergent or convergent tends to be deflected due to the Coriolis effect (see the right panel of Fig. 1 for the illustration). This deflection results in a vorticity that is anticyclonic for divergent flow and cyclonic for convergent flow. In the northern hemisphere, the anticyclonic vorticity is negative, while in the southern hemisphere it is positive. Consequently, we anticipated a negative correlation of the function $\widetilde{C}(\delta, \xi)$ at the stable layer in the northern hemisphere. Conversely, a positive correlation is expected in the southern hemisphere. For the sake of simplicity, hereafter our discussion will be concentrated on the northern hemisphere. In this region, the value of $\widetilde{C}(\delta, \xi)$ is anticipated to be negative within the stable layer.

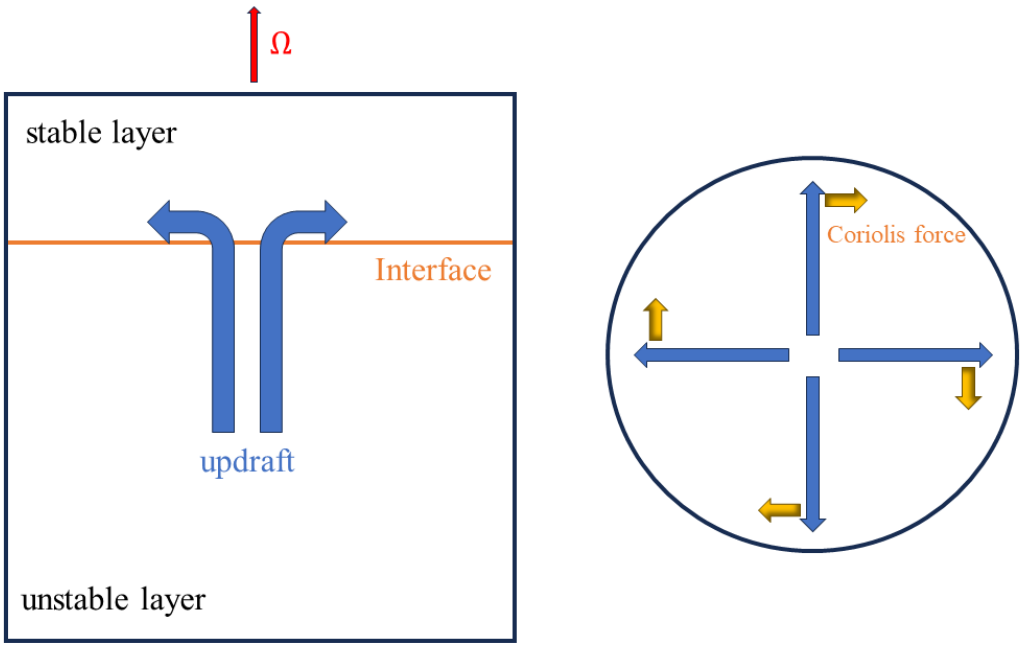

Figure 1. The sketch plots illustrate the horizontal divergence and vertical vorticity near the interface between the convectively unstable and stable layers in the northern hemisphere. The left panel depicts an updraft that diverges (indicating positive horizontal divergence) upon encountering the interface. The right panel depicts that the divergent flow deflects in a clockwise direction (signifying negative vertical vorticity) due to the Coriolis effect.

3 The result

In this study, we use the simulation data of the hexagonal pattern of polar cyclones in Cai et al. (2021) (referred to Case B in that paper). Cai et al. (2021) solve the following hydrodynamic equations of fully compressible flow by large-eddy simulation

$$\partial_t \rho = -\boldsymbol{\nabla} \cdot (\rho \boldsymbol{v}) \ , \tag{4}$$

$$\partial_t (\rho \boldsymbol{v}) = -\boldsymbol{\nabla} \cdot (\rho \boldsymbol{v}\boldsymbol{v}) - \boldsymbol{\nabla} p + \boldsymbol{\nabla} \cdot \boldsymbol{\Sigma} + \rho \boldsymbol{g} + 2\rho \boldsymbol{v} \times \boldsymbol{\Omega} \ , \tag{5}$$

$$\partial_t E = -\boldsymbol{\nabla} \cdot [(E+p)\boldsymbol{v} - \boldsymbol{v} \cdot \boldsymbol{\Sigma} + \boldsymbol{F_d}] + \rho \boldsymbol{v} \cdot \boldsymbol{g} - \rho c_p (T - T_{top})/\tau \ , \tag{6}$$

where ρ, p, T, $\boldsymbol{v}$, E, $\boldsymbol{\Sigma}$, $\boldsymbol{\Omega}$, c_p, $\boldsymbol{g}$, $\boldsymbol{F_d}$, τ are the density, pressure, temperature, velocity, total energy, viscous stress tensor, heat capacity under constant pressure, gravitational acceleration, the diffusive flux, and Newton cooling rate, respectively.

This simulation is performed in a polar gamma box, with a horizontal to vertical aspect ratio λ of 16. This setup spans a colatitude angle θ_c of 12° from the pole. We choose the initial state values of pressure, density, temperature, and height at the top of the box as the reference values. Specifically, the reference values are set as follows: pressure at $p_{top} = 10^5 Pa$, density at $\rho_{top} = 0.167 kg/m^3$, temperature at $T_{top} = 166K$, and height at $H_{top} = 1841km$. All physical variables are then normalized by proper combinations of these reference values. For example, the time can be normalized by $H_{top}(p_{top}/\rho_{top})^{-1/2}$, and the angular velocity can be normalized by $H_{top}^{-1}(p_{top}/\rho_{top})^{1/2}$. The simulation box is structured into two layers: a convectively stable layer above a convectively unstable layer. The initial thermal structure is set to a polytropic state with $\rho = T^n$. In the convectively unstable layer, $n = 2.128$, which is also the value of adiabatic polytropic index n_{ad}. In the convectively stable layer, $n = 9$. The interface between the stable and unstable layers is at the nondimensional height of $z = 0.95$, approximately $90km$ from the top. The non-dimensional angular velocity Ω is set to 0.5, corresponds to a rotation period of $8.3hrs$. Consequently, the non-dimensional Coriolis parameter is 1.0 at the pole. Hereafter, we express our results using nondimensional variables when units are not specified. The simulation employs periodic boundary conditions in the horizontal directions. In the vertical direction, it uses impenetrable boundary condition for velocity, and constant flux and temperature respectively at the bottom and top for the thermal boundaries.

The simulation's grid resolution, denoted as $N_x \times N_y \times N_z$, is set to be $1192^2 \times 129$. Consequently, each grid cell covers approximately 0.02°. For additional details on numerical settings, one can refer to Cai et al. (2021). The velocity field, represented as (u, v, w), was recorded over a duration equivalent to approximately 40 units of planetary rotation periods. Here, u, v, w denotes the velocities along the x-, y-, and z-directions, respectively. Subsequently, the horizontal divergence, represented as $\delta = \partial_x u + \partial_y v$, and the vertical vorticity, represented as $\xi = \partial_x v - \partial_y u$ were computed at each grid point (i, j). This computation was performed using a central finite difference scheme, which incorporates the four neighbouring points $(i-1, j)$, $(i+1, j)$, $(i, j-1)$, $(i, j+1)$.

Fig. 2 presents the three-dimensional structures derived from our simulation results (Cai et al., 2021). The upper-left panel illustrates the structure of horizontal divergence δ. It can be observed from the figure that δ primarily deviates from zero in the vicinity of the convectively stable layer. This deviation is attributed to the tendency of the flow to diverge or converge upon encountering the interface. The upper-right panel depicts the vertical velocity w. It unveils lane structures that align approximately with the rotational axis. Within the cyclones, alternating updrafts and downdrafts are observed in the spiral arms. These stacked vertical flows exhibit a significant positive correlation with δ in the stable layer. Contrary to the structure of δ, the contrast of w from the top to the bottom is less pronounced. The lower-left panel presents the structure of the vertical vorticity. It clearly shows that the large-scale cyclones are deeply rooted, extending vertically from the top all the way down to the bottom. The structures of cyclones

are signified by showing the volume rendering of the vertical vorticity near $\xi = 1$ and $\xi = 3$ in the lower-right panel. Interestingly, the inner cores of these cyclones display a higher vorticity, forming cone-shape structures that extend from the bottom to top. In contrast, the outer cores of these cyclones resemble cylinder-shape strcutres.

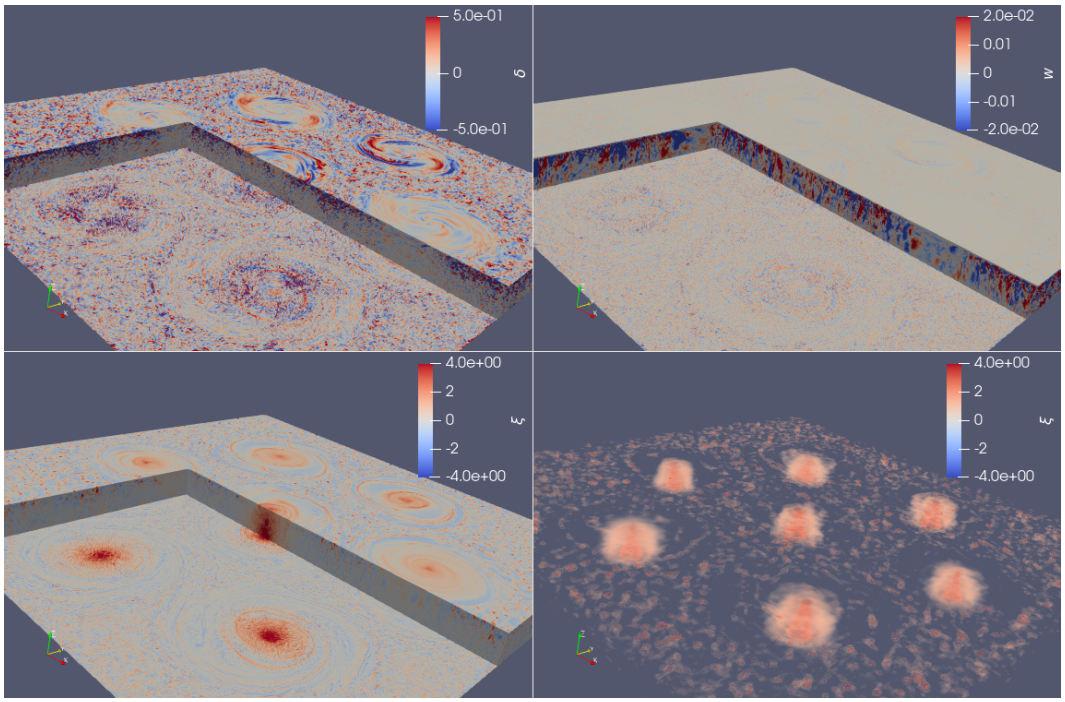

Figure 2. The three-dimensional structures of our simulation result (Cai et al., 2021). The upper-left, upper-right, and lower-left panels show the structures of horizontal divergence, vertical velocity, and vertical vorticity, respectively. The lower-right panel signifies the structures of cyclones by showing the volume renderings of the vertical vorticity near $\xi = 1$ and $\xi = 3$.

3.1 Statistics in the upper stable layer

We begin by examining the statistical behaviour at the height of $z = 0.96$. This location is just above the interface in the stable layer. Figs. 3(a-c) present contour plots of δ, ξ, and w at a height of $z = 0.96$. As observed in Fig. 3(a), δ exhibits a tendency to be positive within the inner core regions of the cyclones. Conversely, in the cyclones' outer rims, δ displays band structures encompassing both positive and negative values. Beyond the confined region of these cyclones, δ exhibits a random distribution of positive and negative values. In Fig. 3(b), ξ predominantly exhibits positive values within the inner core regions and spiral arms. However, regions situated between inner core and spiral arms display blocks of negative ξ values. Beyond the cyclones, ξ manifests a cellular structure characterized by positive lanes interspersed with negative blocks. As depicted in Fig. 3(c), the structure of w is quite similar to that of δ. The inner core regions predominantly exhibit upflows, while the outer rims display banded structures composed of both upflows and downflows. Figs. 3(d-f) depict the interrelationships among δ, ξ, and w by presenting contour plots of their respective products. It is evident in Fig. 3(d) that the product of δ and ξ tends to be negative in areas outside the cyclones. Within the cyclones, positive and negative values of $\delta\xi$ are alternately distributed along the spiral arms. In Fig. 3(e), the product of δ and w exhibits distinct positive values both in the cyclones' rims and areas outside the cyclones. This pattern indicates a strong cor-

relation between these two variables in these regions. However, in the inner core regions of the cyclones, δ and w are largely uncorrelated. As illustrated in Fig. 3(f), the pattern of the product of w and ξ mirrors to that of δ and ξ. This similarity is expected, given the high correlation between w and δ.

Figs. 3(g-l) illustrate the relationships among δ, ξ, and w by presenting their histograms and respective cross-relations. Figs. 3(g-i) show their histograms. The histogram of δ exhibits an approximate symmetry. In contrast, the histogram of ξ distinctly displays a right-skewed distribution, peaking around $\xi = -0.5$ (the value of $-\Omega$). This suggests a higher concentration of values on the negative side, while more extreme values are found on the positive side. Conversely, the histogram of w reveals a right-skewed bimodal distribution, with one peak at zero and the other at a negative value. This suggests that the downward flow is less intense and more dispersed, whereas the upward flow is more potent but localized. Fig. 3(j-l) present the cross-relations of these three variables. As shown in Fig. 3(j), the scatter plot of δ against ξ indeed indicates a negative correlation, with a correlation coefficient of -0.32. Similarly, w and ξ are negatively correlated, with a correlation coefficient of -0.24. However, the correlation between w and δ demonstrates a strong positive correlation, with a correlation coefficient of $+0.5$. These findings align with our previous theoretical analysis.

To enhance our understanding of the cross-relations among these variables, we have partitioned the data into two subsets: one that solely encompasses the cyclones (Fig. 4(a-f)), and the other that omits these cyclones (Fig.4(g-l)). In the first subset, the histogram of ξ illustrated in Fig. 4(b) presents a slightly left-skewed distribution, a characteristic that stands in contrast to the distribution seen in the complete data set displayed in Fig. 3(h). This implies a greater accumulation of positive ξ values within the regions affected by cyclones. Interestingly, w exhibits a nearly symmetric distribution within these cyclone regions (Fig. 4(c)). This observation signifies that the downward and upward flows are almost evenly dispersed within the cyclone-affected areas. The correlations between δ and ξ, and between w and ξ, are considerably less pronounced than those in the entire data set. The correlation coefficients, $C(\delta, \xi)$ and $C(w, \xi)$, are -0.23 and -0.11 respectively, which are remarkably lower than their counterparts in the comprehensive data set. This could likely be attributed to the substantial suppression of convective motion within the areas affected by cyclones (K. L. Chan & Mayr, 2013). Fig. 4(g-l) displays the related histograms and cross-correlations for the secondary subset. Both ξ and w exhibit right-skewed distributions, suggesting that the right skewness observed in the comprehensive data set is primarily attributable to this secondary subset. Unexpectedly, our analysis reveals that instances of extreme vorticity are more frequently observed outside the cyclone regions (Fig. 4(h)), rather than within them (Fig. 4(b)). The correlation coefficients $C(\delta, \xi)$ and $C(w, \xi)$ closely matched those calculated in the complete data set. This reaffirms that their negative correlations are primarily driven by the data outside the cyclone regions. The correlation coefficient $C(w, \delta)$ remains nearly constant, irrespective of whether it is inside or outside the cyclone regions. This is reasonable, given their close interrelation via the principle of mass conservation.

The scales of motion are larger within cyclones than outside of them. We can now examine how these scales of motion influence the histograms and correlations. The peak at $\xi = -0.5$ in the histogram of ξ depicted in Fig. 3(h) is attributed to the small-scale flows occurring outside the cyclones. The minor bump at $\xi = 1$ is due to large-scale flows within the cyclones, as demonstrated in the lower-right panel of Fig. 2 and Fig. 4(b). In the lower-right panel of Fig. 2, we also noted that high positive vorticity can either be concentrated in the cyclone's inner core or distributed dispersedly outside the cyclones. Consequently, the extended tail on the right side of ξ in Fig. 3(h) can be ascribed to both intra-cyclonic and extra-cyclonic activities. The peak value at $w = 0$ in Fig. 3(i) is ascribed to intra-cyclonic movements, while the peak of w at the negative value is linked to extra-cyclonic movements. Updrafts and downdrafts are nearly uniformly distribut-

ed within cyclones. However, outside cyclones, the distribution is skewed, with more pronounced updrafts and less intense downdrafts. The correlation between w and ξ is less pronounced within cyclones than outside of them. Within cyclones, the negative correlation between w and ξ is primarily due to the spiral arms, as illustrated in Fig. 2. Outside of cyclones, a substantial negative correlation between w and ξ is observed for small-scale flows.

3.2 Statistics in the lower unstable layer

Similar to Fig. 3, we have depicted the corresponding contour plots at the height of z=0.5 in Figs. 5(a-f). In the middle of the convection zone, the flow exhibits less divergence or convergence compared to the conditions at z=0.96. This is expected due to the lack of an interface that would force the updraft or downdraft to change direction. The pattern of vorticity is more concentrated within the inner regions of cyclones, which are marked by reducing spiral arms. Previous discussions indicate that upflows are predominantly concentrated in the inner regions at z=0.96. However, at z=0.5, both upflows and downflows can be observed within the inner regions of cyclones. The value of $\delta\xi$ deviates from zero only around the cyclone centers, which is a contrast to the conditions at z=0.96, where it deviates from zero both inside and outside the cyclones. The correlation between δ and w is not significant, which is markedly different from the conditions at z=0.96, where a strong correlation between δ and w is observed. The correlation between ξ and w exhibits a strong relationship within the core areas, with both positive and negative values.

Similarly, we have illustrated the histograms and correlations among δ, ξ, and w in Figs. 5(g-l). Each histogram displays only a minor skewness. Moreover, the correlations among these variables are weak, with $C(\delta,\xi) = -0.11$ and $C(w,\xi) = C(w,\delta) = -0.06$. It's worth noting that the correlation between w and δ is negative, which is in stark contrast to the situation at $z = 0.96$, where a strong positive correlation is observed. Furthermore, the correlation coefficient between δ and ξ is considerably smaller that at $z = 0.96$. This suggests that the relation between δ and ξ can be insignificant in the convection zone, despite the fact that the cyclones are propelled by convection.

3.3 Comparison to observation

In previous discussion, we have examined the distribution and correlations between divergence and vorticity at a specific moment, mirroring the approach taken in the observation study by Ingersoll et al. (2022). The time dependency of this correlation warrants further investigation. Fig. 6(a) illustrates the value of $C(\delta,\xi)$ at $z = 0.96$ as a function of time. The figure reveals that $C(\delta,\xi)$ remains relatively stable over time, suggesting a robust correlation. In addition to temporal evolution we have also explored the effect of spatial resolution. To scrutinize the impact of resolution, we select grids $(i-s,j)$, $(i+s,j)$, $(i,j-s)$, and $(i,j+s)$ as neighboring grids when calculating δ and ξ. When $s = 1$, the resolution for δ and ξ is about $50km$. For a larger s, the resolution will be $s\times 50km$. We have computed $C(\delta,\xi)$ by varying both s and z, with the results displayed in Fig. 6(b). The figure indicates that both height and resolution significantly influence $C(\delta,\xi)$.

The strongest correlation of $C(\delta,\xi)$ is detected near the interface between the convectively unstable and stable layers. The correlation coefficient decreases rapidly above this interface. Ingersoll et al. (2022) employed the infrared image of the JIRAM M band to track clouds, corresponding to a depth of roughly $50km$. Considering that this is merely halfway to the interface, we expect that the signature for the correlation between divergence and vorticity is not substantial. Furthermore, the figure also indicates that the magnitude of $C(\delta,\xi)$ diminishes with a decrease in resolution. In proximity to the in-

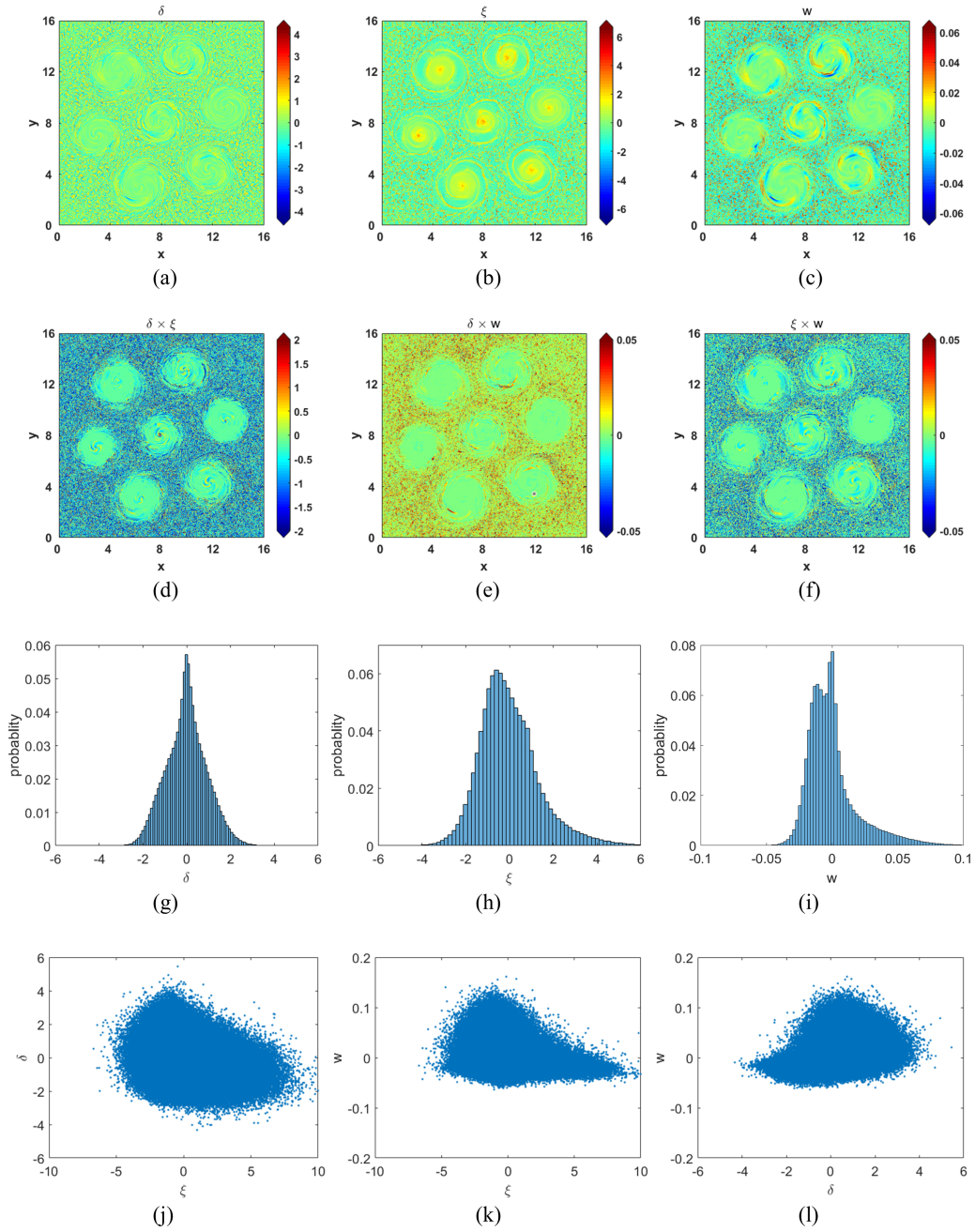

Figure 3. The first row displays contour plots of the horizontal divergence (δ), the vertical vorticity (ξ), and the vertical velocity (w). The second row illustrates contour plots of their respective products, namely $\delta\xi$, δw, and ξw. The third row shows the histograms of δ, ξ, and w. The fourth row shows their cross-relations. The correlation coefficients for δ and ξ, w and ξ, and w and δ are -0.32, -0.24, and +0.5, respectively. The selected data corresponds to a height of $z = 0.96$, slightly above the interface between the convectively unstable and stable layers.

terface, $C(\delta, \xi)$ has decreased by a factor of 1/3 when the resolution is reduced from $50km$ to $300km$. Away from the interface, the signature for $C(\delta, \xi)$ is even less profound when

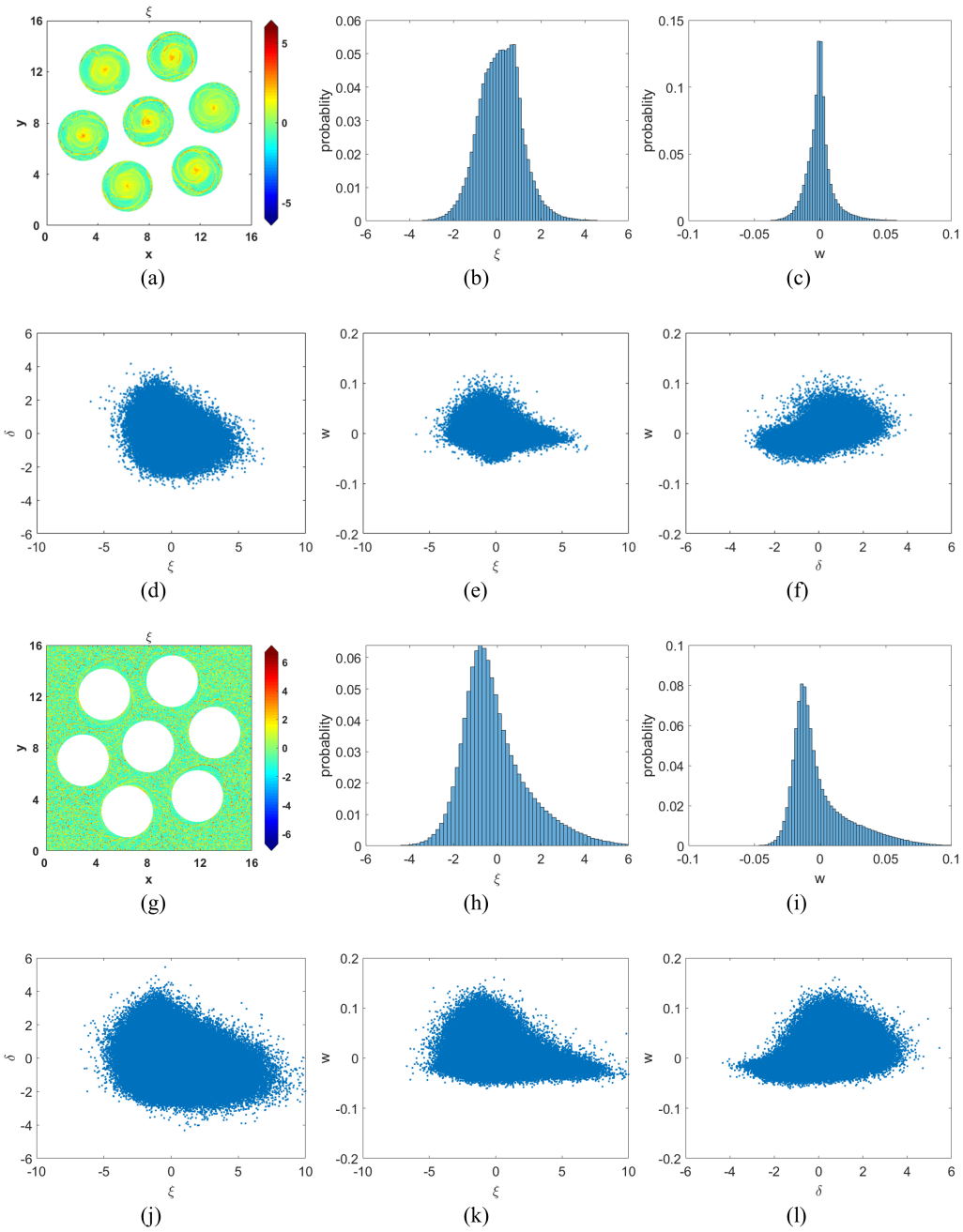

Figure 4. Analogous to Fig. 3. The first two rows only take into account the data within the cyclones. The correlation coefficients for δ and ξ, w and ξ, and w and δ are -0.23, -0.11, and +0.49, respectively. The last two rows only take into account the data outside the cyclones. The correlation coefficients for δ and ξ, w and ξ, and w and δ are -0.34, -0.26, and +0.5, respectively.

a lower resolution is utilized. This likely explains why Ingersoll et al. (2022) did not detect a significant signal for the correlation between divergence and vorticity.

In our analysis, we used data from the entire plane. However, due to the limited field of view of JIRAM, the observed image only contains three cyclones (Ingersoll et al.,

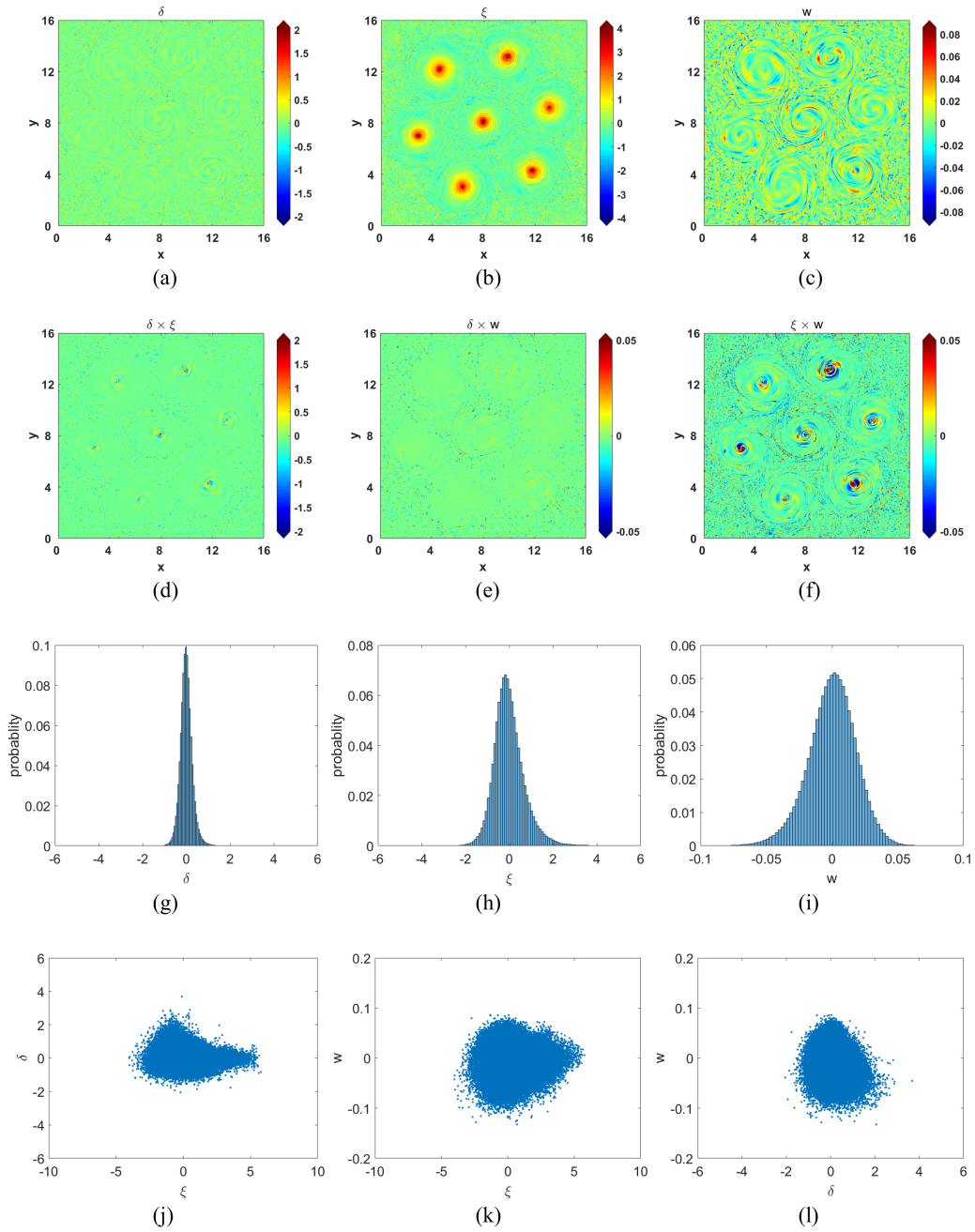

Figure 5. The first row displays contour plots of the horizontal divergence (δ), the vertical vorticity (ξ), and the vertical velocity (w). The second row illustrates contour plots of their respective products, namely $\delta\xi$, δw, and ξw. The third row shows the histograms of δ, ξ, and w. The fourth row shows their cross-relations. The correlation coefficients for δ and ξ, w and ξ, and w and δ are -0.11, -0.06, and -0.06, respectively. The selected data corresponds to a height of $z = 0.5$, at the middle of the convection zone.

2022). Given that the correlation can vary among different cyclones, it becomes necessary to conduct a sensitivity analysis to understand the dependence of the correlation

on each individual cyclone. In Fig. 7, we computed the correlations by analyzing distinct regions: each cyclone independently and the region excluding all cyclones. The correlations within individual cyclones show sensitivity in the convectively unstable layer, yet they consistently follow a similar trend in the convectively stable layer, marked by a dip near the unstable-stable interface. Interestingly, the correlation in the region excluding all cyclones aligns with that computed for the entire horizontal plane. This suggests that the correlation is primarily influenced by points outside the cyclones. Given that all patterns exhibit a dip near the interface, it is reasonable to infer that the divergence and vorticity are correlated in the stable layer, irrespective of whether they are inside or outside cyclones.

Siegelman, Klein, et al. (2022) utilized a geostrophic model in conjunction with infrared bright temperature data to estimated the correlation between divergence and vorticity. They have discovered a negative correlation between these two factors at a scale of approximately $100km$. Additionally, they observed an upscale energy transfer from scales smaller than roughly $200km$ to larger scales. Ingersoll et al. (2022) questioned the validity of the geostrophic approximation on the application to Jovian atmosphere. According to the geostrophic approximation, if it holds true, then ξ should be much less than f, leading to the balance of the vorticity equation $D_t\xi \approx -f\delta$. However, simulations indicate that the magnitude of ξ can significantly exceed f (where $f \approx 1$ in our simulation). This finding challenges the validity of the geostrophic approximation. In addition, the horizontal average value $\overline{D_t\xi}$ should approach to zero under the geostrophic approximation, given that $f\delta$ is a linear term. However, our simulation shows that $\overline{D_t\xi}$ is significantly different from zero, especially in the convectively stable layer.

By taking a horizontal average of the vorticity equation, $\overline{D_t\xi}$ can be expressed as

$$\overline{D_t\xi} = \underbrace{\overline{(\boldsymbol{\xi}_h \cdot \boldsymbol{\nabla}_h)w}}_{\text{tilting term}} - \underbrace{\overline{\xi}\overline{\delta}}_{\text{stretching term}} + \underbrace{\overline{\rho^{-2}\boldsymbol{\nabla}_h\rho \times \boldsymbol{\nabla}_h p}}_{\text{baroclinic term}} . \tag{7}$$

The above equation indicates that $\overline{D_t\xi}$ is, in fact, balanced by three nonlinear terms: the stretching term, the tilting term, and the baroclinic term. We have depicted the horizontal averages of these three terms, along with their collective contribution, in Fig. 6(c). We note that the baroclinic term is relatively insignificant. The net contribution, equivalent to $\overline{D_t\xi}$, is distinctly nonzero in the upper stable layer, as the stretching term and the tilting term are not in balance. The tilting effect is more pronounced in the unstable layer, whereas the stretching effect dominates in the stable layer. The cumulative result is a transfer of vorticity from the unstable layer to the stable layer. In this study, our focus is solely on the transport of vertical vorticity. The baroclinic term in this context only encompasses the horizontal gradients of pressure and density. When observed in a horizontal plane, the contours of pressure and density within cyclones are nearly parallel. As a result, the baroclinic term's contribution to the transfer of vertical vorticity is negligible. However, as depicted in Fig. 2, the cyclone structures within the compressible flow exhibit baroclinicity. This baroclinicity could potentially contribute to the transfer of horizontal vorticities.

Siegelman, Klein, et al. (2022) observed an upscale energy cascade from small scales to large scales. We have computed the compensated horizontal kinetic energy spectra as a function of wavenumber. As the z-direction is aperiodic, we define the two-dimensional horizontal kinetic energy spectrum $P_{2h}(k)$, as per K. L. Chan and Sofia (1996) and Cai et al. (2022), as follows:

$$\int P_{2h}(k)dk = \sum_m \sum_n (|v_{x,mn}|^2 + |v_{y,mn}|^2) . \tag{8}$$

Here the subscripts m, n represent the wavenumber in the x, y-directions, respectively. $k = \lfloor (m^2+n^2)^{1/2} \rfloor$ is the horizontal wavenumber. We then use the compensated hori-

zontal kinetic energy spectrum $kP_{2h}(k)$ to approximate the three-dimensional kinetic energy spectrum.

In the simulation of the Great Red Spot, Cai et al. (2022) observed an upscale energy transfer. Here again, we observe a similar upscale energy transfer occurs in the simulation of polar cyclones. For wavenumbers $k \leq 30$, the spectra remain almost identical at different heights. This suggests that large-scale cyclones are maintained by the same mechanism, an upscale energy transfer, across both unstable and stable layers. In the stable layer, kinetic energy decays more rapidly at small scales. Deep atmospheric convection supplies the energy required for this decay in the stable layer.

To further investigate the energy transfer within the cyclone, we selected a small region, with a horizonal size of 2×2, only encompassing the central cyclone. The kinetic energy spectrum of this confined space was computed and is illustrated in Fig. 6(e). The data reveals a clear inverse cascade of upscale energy transfer within the cyclone. Also apparent is the forward energy cascade from medium scales ($k > 10$) to smaller scales. However, we have not observed significant dissipation at the smallest scales at the top of the stable layer. This leads us to consider two possibilities. The first possibility is that the energy at small scales is transferred outside the cyclone, where it subsequently dissipates. The second possibility is that our resolution within the cyclone is insufficient to resolve the small-scale dissipations. Resolving small-scale dissipation is computationally demanding. We leave it to future studies.

In the study by Cai et al. (2021), two cases of Jupiter's polar cyclones were computed: one exhibiting a hexagonal pattern and the other, a pentagonal pattern. This paper conducts a comprehensive analysis of the hexagonal pattern case, revealing a substantial negative correlation between divergence and vorticity. We then extend our investigation to the pentagonal pattern to ascertain if the same correlation holds true. As illustrated in Fig.6(f), we examine the dependence of $C(\delta, \xi)$ on both the height z and resolution step s. The findings align closely with those of the hexagonal case, suggesting that the results are robust, provided the driving mechanisms of the polar cyclones remain consistent.

4 Summary

In rotating convection, theory suggests a negative correlation between divergence and vorticity in the northern hemisphere, and a positive correlation in the southern hemisphere. This relationship serves as a signature for convection. This theory has been validated by observational data from solar convection. Given the Sun's slow rotation, solar convection is characterized by granular cells with converging downflows and diverging upflows. These flows, deflected by the Coriolis force, result in vertical vorticity. Consequently, there is a strong correlation between horizontal divergence and vertical vorticity. However, Jupiter's rotation is significantly faster than the Sun's, and the Jovian atmospheric flow pattern is characterized by jets and large-scale vortices. The applicability of the theory to Jupiter is still a matter of debate. Ingersoll et al. (2022) investigated the relationship between divergence and vorticity for Jupiter's polar cyclones, but they did not find any significant correlations. Conversely, Siegelman, Klein, et al. (2022) identified a correlation using a geostrophic model. This discrepancy raises questions about whether convection is responsible for sustaining Jupiter's polar cyclones.

In our previous three-dimensional simulation of deep rotating convection, we discovered that Jupiter's polar cyclones can be naturally produced by convection. In this study, we have examined the relationship between divergence and vorticity using the data from our simulation. Our findings confirm the theoretical prediction of a negative correlation between divergence and vorticity in the stable layer of the northern atmosphere. This correlation is less pronounced within the cyclones compared to outside them. We

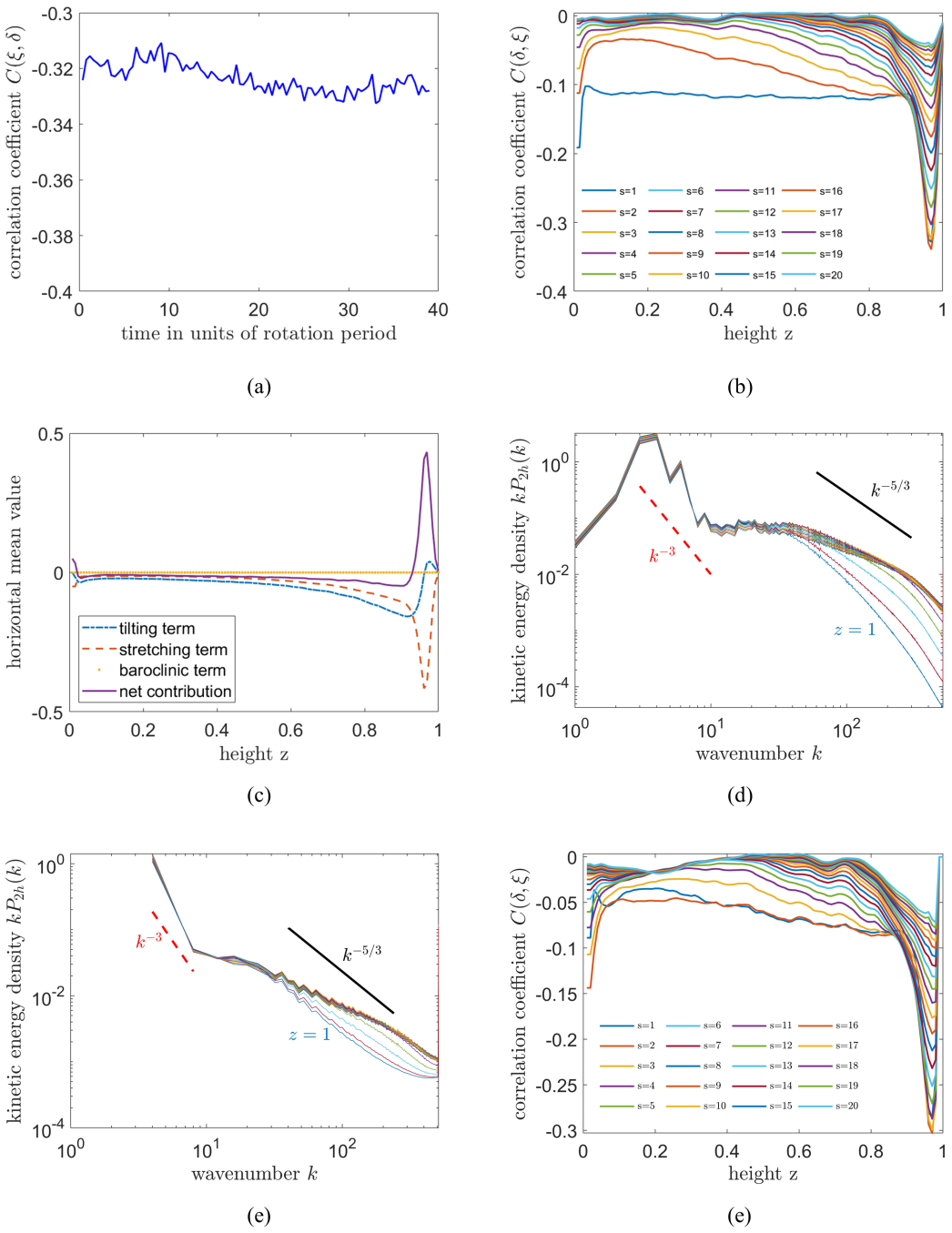

Figure 6. (a)The time evolution of $C(\delta,\xi)$ at $z = 0.96$, which indicates a stable correlation between divergence and vorticity. (b)The dependence of $C(\delta,\xi)$ on height z and resolution step s. The resolution for calculating δ and ξ is $s \times 50km$. (c)The distributions of horizontally averaged stretching term, tilting term, baraclinic term, and their net contribution (tilting term - stretching term + baroclinic term). (d)The kinetic energy spectrums as functions of wavenumbers at different heights $0.9 \leq z \leq 1$. The spectrum decays more rapid at small scales with higher height. (e)The kinetic energy spectrums in a small region with a size of 2×2, only encompassing the central cyclone. (f)The dependence of $C(\delta,\xi)$ on height z and resolution step s for the case of pentagonal pattern in Cai et al. (2021). The resolution for calculating δ and ξ is $s \times 100km$.

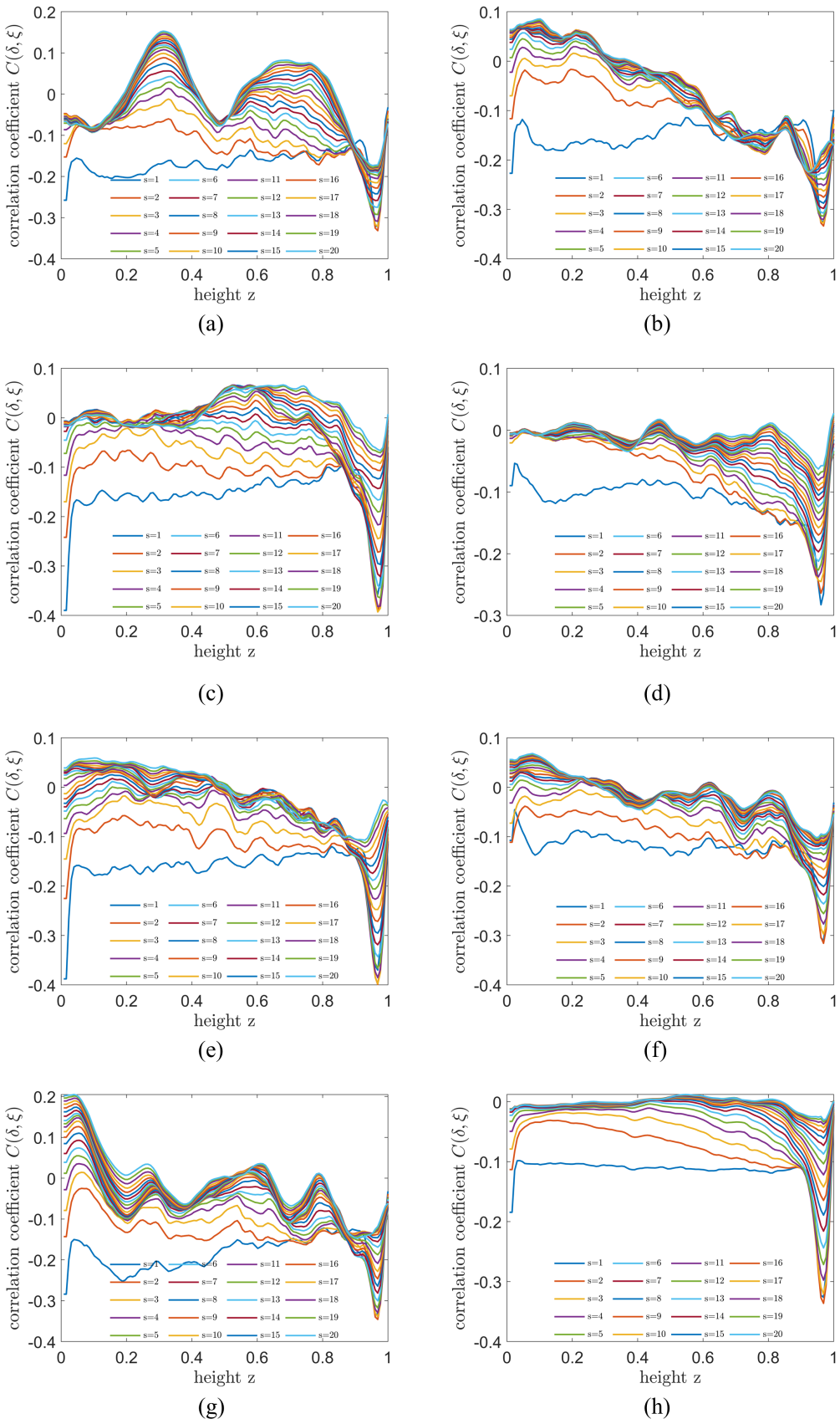

Figure 7. The dependence of $C(\delta,\xi)$ on height z and resolution step s. (a-g)$C(\delta,\xi)$ for regions of each independent cyclone, respectively. (h)$C(\delta,\xi)$ for the region excluding all the cyclones. The resolution for calculating δ and ξ is $s \times 50km$.

also observed a significant skewness in the vorticity distribution, primarily contributed by the areas outside the cyclones. Within the cyclones, upflows and downflows are nearly evenly distributed. However, outside the cyclones, the distribution of vertical velocity is significantly skewed to the right. This suggests that the skewness of upflows and downflows plays a crucial role in the relationship between divergence and vorticity. In the middle of the convection zone, the vorticity and vertical velocity are only slightly skewed, resulting in a weak correlation between divergence and vorticity.

We observe that the correlation between divergence and vorticity is significantly influenced by both the height and resolution. A strong correlation is evident near the interface between the unstable and stable layers, but this correlation diminishes rapidly as we move away from the interface. The resolution used in computing divergence and vorticity also has a substantial impact on the correlation, with the correlation decaying quickly as the resolution is reduced. Ingersoll et al. (2022) utilized data from the JIRAM M band to compute divergence and vorticity. However, the penetrative depth of the JIRAM M band is approximately 50 km, which only reaches halfway to the interface. Furthermore, the resolution of the JIRAM M band is insufficient. As a result, they were unable to identify a signature for the correlation.

Siegelman, Klein, et al. (2022) employed a geostrophic model to interpret the observational data. However, our findings cast doubt on the validity of this model. Our simulation data indicates that vorticity is either comparable to or exceeds the Coriolis parameter, contradicting the geostrophic approximation's assumption of diminishing vorticity. Furthermore, we discovered that the horizontal average of the material derivative of vorticity is not zero in the stable layer. The material derivative of vorticity is influenced by both stretching and tilting effects. In the stable layer, the stretching effect is dominant, while the tilting effect prevails in the unstable layer. These findings suggest a transfer of vorticity from the convectively unstable layer to the stable layer by the tilting and stretching effects. Our simulations also reveal the occurrence of an inverse cascade, which aligns with the analysis of observed data.

In conclusion, it is essential to compare our findings with those observed in solar convection. Gizon and Duvall Jr (2003) reported a correlation of a few percent between divergence and vorticity at the Solar surface. This correlation is significantly smaller than the value obtained from our simulation at the interface. However, it aligns in magnitude with the value from our simulation at the top of the box. These results suggest that divergence and vorticity are likely to be correlated in both slowly and rapidly rotating convection. Gizon and Duvall Jr (2003) also demonstrated that this correlation varies with latitude in solar convection, with the highest values observed at the poles and zero at the equator. It would be intriguing to compare the correlation of Jovian convection with that of Solar convection at different latitudes. A global simulation, or comprehensive observation of Jupiter's atmosphere, could provide valuable insights into this matter.

China is planning to initiate the Tianwen-4 mission aimed at exploring the Jovian system. The inclusion of payloads with enhanced horizontal resolutions and deeper filters could potentially address this issue in the future.

Data Availability Statement

The data and code utilized in the creation of the figures, inclusive of the vtr files for three-dimensional structures, can be accessed in the figshare repository Cai (2024). The figures were produced using the software Matlab and Paraview.

Acknowledgments

I thank Andrew Ingersoll and the other anonymous reviewer for the helpful comments. I am grateful to Kwing L. Chan for the fruitful discussion in rotating convection of planetary atmospheres. This work has been supported by the National Natural Science Foundation of China (No. 12173105), and Guangdong Basic and Applied Basic Research Foundation (No. 2414050002575).

References

Adriani, A., Mura, A., Orton, G., Hansen, C., Altieri, F., Moriconi, M., ... others (2018). Clusters of cyclones encircling jupiter's poles. *Nature*, *555*(7695), 216–219.

Brueshaber, S. R., Sayanagi, K. M., & Dowling, T. E. (2019). Dynamical regimes of giant planet polar vortices. *Icarus*, *323*, 46–61.

Brummell, N. H., Hurlburt, N. E., & Toomre, J. (1996). Turbulent compressible convection with rotation. i. flow structure and evolution. *The Astrophysical Journal*, *473*(1), 494.

Cai, T. (2016). A semi-implicit spectral method for compressible convection of rotating and density-stratified flows in cartesian geometry. *Journal of Computational Physics*, *310*, 342–360.

Cai, T. (2021). Large-scale vortices in rapidly rotating rayleigh–bénard convection at small prandtl number. *The Astrophysical Journal*, *923*(2), 138.

Cai, T. (2024). Data for "examination of vorticity and divergence on a rotating turbulent convection model of jupiter's polar vortices". *figshare*. Retrieved from `https://doi.org/10.6084/m9.figshare.24944064.v2`

Cai, T., Chan, K. L., & Chow, K.-C. (2022). Spontaneous generated convective anticyclones at low latitudea model for the great red spot. *The Astrophysical Journal*, *925*(1), 94.

Cai, T., Chan, K. L., & Mayr, H. G. (2021). Deep, closely packed, long-lived cyclones on jupiters poles. *The Planetary Science Journal*, *2*(2), 81.

Chan, K. (2007). Rotating convection in f-boxes: Faster rotation. *Astronomische Nachrichten*, *328*(10), 1059.

Chan, K. L., & Mayr, H. G. (2013). Numerical simulation of convectively generated vortices: Application to the jovian planets. *Earth and Planetary Science Letters*, *371*, 212–219.

Chan, K. L., & Sofia, S. (1996). Turbulent compressible convection in a deep atmosphere. v. higher order statistical moments for a deeper case. *Astrophysical Journal v. 466, p. 372*, *466*, 372.

Egorov, P., Rüdiger, G., & Ziegler, U. (2004). Vorticity and helicity of the solar supergranulation flow-field. *Astronomy & Astrophysics*, *425*(2), 725–728.

Favier, B., Silvers, L. J., & Proctor, M. R. (2014). Inverse cascade and symmetry breaking in rapidly rotating boussinesq convection. *Physics of Fluids*, *26*(9).

Gizon, L., & Duvall Jr, T. (2003). Supergranulation supports waves. In *Gong+ 2002. local and global helioseismology: The present and future* (Vol. 517, pp. 43–52).

Guervilly, C., Hughes, D. W., & Jones, C. A. (2014). Large-scale vortices in rapidly rotating rayleigh–bénard convection. *Journal of Fluid Mechanics*, *758*, 407–435.

Hathaway, D. H. (1982). Nonlinear simulations of solar rotation effects in supergranules. *Solar Physics*, *77*, 341–356.

Ingersoll, A. P., Ewald, S. P., Tosi, F., Adriani, A., Mura, A., Grassi, D., ... others (2022). Vorticity and divergence at scales down to 200 km within and around the polar cyclones of jupiter. *Nature Astronomy*, *6*(11), 1280–1286.

Julien, K., Rubio, A. M., Grooms, I., & Knobloch, E. (2012). Statistical and physical balances in low rossby number rayleigh–bénard convection. *Geophysical & Astrophysical Fluid Dynamics*, *106*(4-5), 392–428.

Käpylä, P. J., Mantere, M. J., & Hackman, T. (2011). Starspots due to large-scale vortices in rotating turbulent convection. *The Astrophysical Journal*, *742*(1), 34.

Komm, R., Howe, R., & Hill, F. (2021). Divergence and vorticity of subsurface flows during solar cycles 23 and 24. *Solar Physics*, *296*, 1–27.

Komm, R., Howe, R., Hill, F., Miesch, M., Haber, D., & Hindman, B. (2007). Divergence and vorticity of solar subsurface flows derived from ring-diagram analysis of mdi and gong data. *The Astrophysical Journal*, *667*(1), 571.

Kunnen, R. P., Ostilla-Mónico, R., Van Der Poel, E. P., Verzicco, R., & Lohse, D. (2016). Transition to geostrophic convection: the role of the boundary conditions. *Journal of Fluid Mechanics*, *799*, 413–432.

Li, C., Ingersoll, A. P., Klipfel, A. P., & Brettle, H. (2020). Modeling the stability of polygonal patterns of vortices at the poles of jupiter as revealed by the juno spacecraft. *Proceedings of the National Academy of Sciences*, *117*(39), 24082–24087.

O'Neill, M. E., Emanuel, K. A., & Flierl, G. R. (2015). Polar vortex formation in giant-planet atmospheres due to moist convection. *Nature Geoscience*, *8*(7), 523–526.

Rubio, A. M., Julien, K., Knobloch, E., & Weiss, J. B. (2014). Upscale energy transfer in three-dimensional rapidly rotating turbulent convection. *Physical review letters*, *112*(14), 144501.

Rüdiger, G., Brandenburg, A., & Pipin, V. (1999). A helicity proxy from horizontal solar flow patterns. *Astronomische Nachrichten: News in Astronomy and Astrophysics*, *320*(3), 135–140.

Siegelman, L., Klein, P., Ingersoll, A. P., Ewald, S. P., Young, W. R., Bracco, A., ... others (2022). Moist convection drives an upscale energy transfer at jovian high latitudes. *Nature Physics*, *18*(3), 357–361.

Siegelman, L., Young, W. R., & Ingersoll, A. P. (2022). Polar vortex crystals: Emergence and structure. *Proceedings of the National Academy of Sciences*, *119*(17), e2120486119.

Tabataba-Vakili, F., Rogers, J., Eichstädt, G., Orton, G., Hansen, C., Momary, T., ... others (2020). Long-term tracking of circumpolar cyclones on jupiter from polar observations with junocam. *Icarus*, *335*, 113405.

Wang, Y., Noyes, R. W., Tarbell, T. D., et al. (1995). Vorticity and divergence in the solar photosphere. *Astrophysical Journal v. 447, p. 419*, *447*, 419.

Yadav, R. K., & Bloxham, J. (2020). Deep rotating convection generates the polar hexagon on saturn. *Proceedings of the National Academy of Sciences*, *117*(25), 13991–13996.

Zhang, X., & Showman, A. P. (2014). Atmospheric circulation of brown dwarfs: jets, vortices, and time variability. *The Astrophysical Journal Letters*, *788*(1), L6.